

Short-Range Demonstrations of Monocular Passive Ranging Using O_2 ($X^3\Sigma_g^- \rightarrow b^1\Sigma_g^+$) Absorption Spectra

Michael R. Hawks,^a R. Anthony Vincent,^b Jacob Martin,^a Glen P. Perram^{a,*}

^a Department of Engineering Physics, Air Force Institute of Technology Wright-Patterson Air Force Base, Dayton, OH 45433 USA

^b Department of Physics, US Air Force Academy, Colorado Springs, CO 32909 USA

The depth of absorption bands in observed spectra of distant, bright sources can be used to estimate range to the source. Experimental results are presented based on observations of the O_2 $X(v''=0) \rightarrow b(v'=0)$ absorption band centered around 762 nm and the O_2 $X(v''=0) \rightarrow b(v'=1)$ band around 689 nm. Range is estimated by comparing observed values of band-average absorption against predicted curves derived from either historical data or model predictions. Accuracy of better than 0.5% was verified in short-range (up to 3 km), static experiments using a high-resolution (1 cm^{-1}) spectroradiometer. This method was also tested against the exhaust plume of a Falcon 9 rocket launched from Cape Canaveral, Florida. The rocket was launched from an initial range of 13 km and tracked for 90 s after ignition. Range error was below 2% for the first 30 s and consistent with predicted error throughout the track.

Index Headings: Atmospheric absorption; Passive ranging; Molecular oxygen; Target location; Target tracking.

INTRODUCTION

Systems intended to track accelerating targets require measurements to support estimates of each orthogonal coordinate. For many applications this usually means active sensors such as radar or optical analogs (laser radar). For systems intended for flight, active systems have significant drawbacks, since the physical sensing suffers from geometric spreading and path absorption in both directions, necessitating significant power and aperture (with attendant mass) to overcome this inverse range to the fourth power scaling. For example, the track illuminator laser for the Airborne Laser requires a kilowatt-class laser projected through a 1.5 m aperture.¹ Passive sensors require less power, scale inversely with range squared, and might be expected to cover a larger area. However, traditional passive sensors do not provide range estimates. Multisensor triangulation is effective for providing a full three-dimensional (3-D) target location, but this requires a network of sensors that may be costly to maintain and complex to operate. Triangulation can be particularly challenging for fast-moving targets when multiple sensors attempt to quickly acquire and track the same object. A single passive sensor capable of autonomously providing 3-D target location would either enable or greatly simplify several applications.²⁻³

Many passive ranging techniques have been proposed,⁴⁻⁵ but most are intended for close-range applications such as autonomous navigation or process control. For long-range airborne applications, techniques based on atmospheric absorption are most promising. Absorption-based ranging techniques require a broadband emissive target such as a

rocket exhaust plume or other combustion source. Uncertainty in source spectral signatures and solar scatter can degrade the accuracy of range estimates. The state of the atmosphere along the observation path must be known or estimated, including any variations in specie mixing ratios.

We address a method and means of passive range estimation via application of the differential absorption of the spectral radiance of the accelerating target through the intervening atmosphere. Differential absorption can be estimated simply with as few as two well-chosen spectral bands.⁶ Early monocular passive ranging was developed using the mid-infrared CO_2 bands.⁶ Range accuracy from these techniques in the field was limited to $>5\%$. The work presented here explores the benefits of using high-resolution spectra, and focuses on the $O_2(X \rightarrow b)$ bands near 689 and 762 nm.⁷⁻⁸ Oxygen is chosen because it is mixed more uniformly in the atmosphere and is less dependent on weather conditions than most atmospheric absorbers.⁷ Second, the bands are well separated from other atmospheric absorption bands, which simplifies analysis.⁸ Third, many combustion sources will contain hot atmospheric gases, selectively emitting light into the absorption bands we hope to monitor. Hot, unburned oxygen, on the other hand, is rare in combustion plumes. Last, the $O_2(X \rightarrow b)$ bands are based on very weak magnetic dipole transitions, which will reduce the effects of saturation at long ranges.

Experiments. Emission spectra in the visible and near infrared were observed using high-speed Fourier transform spectrometers (FTS). The newer Bomem MR-304 spectrometer provides spectral resolutions of $1\text{--}16\text{ cm}^{-1}$ at rates of $10\text{--}82\text{ Hz}$. An older Bomem MR-254 spectrometer was used for the earlier tests, with scan rates limited to 64.4 s at 16 cm^{-1} . The spectral resolution was typically chosen as 4 cm^{-1} , although experiments show the results are largely independent of instrument resolution.⁹⁻¹⁰ The instrument field of view (FOV) was 4.9 mrad , although smaller field stops were sometimes used to limit the background light. A video camera boresighted to the instrument was used to ensure the source was not clipped by the field stop. The silicon detector with response in the $8500\text{--}15\,000\text{ cm}^{-1}$ range exhibits a rather poor noise equivalent spectral radiance of $\sim 10\text{ }\mu\text{W}/\text{cm}^2\text{ str cm}^{-1}$. The net throughput of the optical system is 27%. Narrow band filters were used in some tests to reduce out-of-band noise and to increase the coherence length of the light, but no clear improvement in the data was observed.

Initial experiments were conducted by observing a 500 W quartz-tungsten-halogen lamp with a 75 mm long element and a crude metallic reflector to direct the light into a solid angle of roughly $2\text{--}2.5$ steradians. The lamp was observed at multiple ranges up to 200 m to test and verify instrument performance and range estimation algorithms. Multiple scans (typically

Received 2 April 2012; accepted 20 December 2012.

* Author to whom correspondence should be sent. E-mail: glen.perram@afit.edu

DOI: 10.1366/12-06673

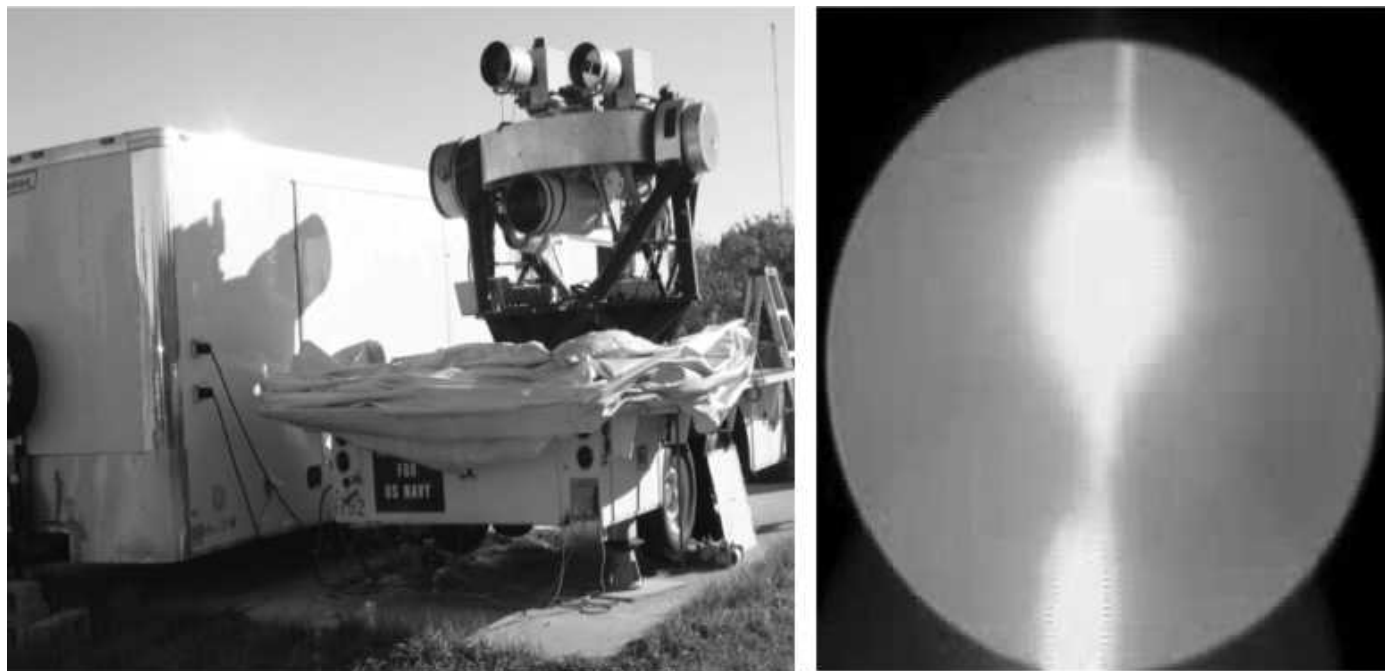


FIG. 1. (Left) AFIT remote sensing trailer next to ISTEf's Black Mace mount. (Right) View through the video camera boresighted through the MR-304, taken 40 s after liftoff. The rocket body is visible at the top of the frame.

100–1000) were co-added with spectral resolutions of 1–32 cm^{-1} .

The method was then applied to three static solid rocket motor (SRM) tests to demonstrate the technique with representative targets. In 2005, the firing of a large, horizontal motor was observed at Edwards Air Force Base, California. The MR-254 spectrometer operating at 2 cm^{-1} resolution was located on a hill overlooking the motor at a slant path distance of 2.82 km (Global Positioning System [GPS] measurements) and at an aspect angle of roughly 75° off-nose. The rocket motor burned for approximately 90 s. In 2010 to 2011, two additional static solid rocket motor firings were observed in the western United States. The MR-304 spectrometer operating at 1 cm^{-1} resolution (10 Hz) with a 76 mrad FOV was located on a hill overlooking the motor at a slant path distance of 900 ± 45 m during a 35 s burn. Meteorological data were recorded locally with a mobile Kestrel weather station.

To validate passive ranging concept at longer ranges and against moving targets, the MR-304 spectrometer was installed on the Black Mace tracking mount at the Innovative Science and Technology Experimentation Facility (ISTEF), on Cape Canaveral, to observe a Falcon 9 launch. The liquid oxygen–kerosene motor represents a significantly different spectral source than the static rocket motor tests with low alkali and high soot content. The mount, shown in Fig. 1, is equipped with 24-bit encoders sampled at 100 Hz and referenced to GPS time. Acquisition and tracking cameras are suspended beneath a large optics bench, with the top surface (roughly 1.2 m diameter) available to mount customer instruments. The mount control computer was programmed to follow a planned trajectory, with corrections applied by an operator. All instrument control computers and operators were housed in the Air Force Institute of Technology (AFIT) remote sensing trailer, positioned next to the mount. The mount control computers and operator were housed in a separate trailer, not

visible in Fig. 1. The mount was located about 13 km from the launch complex.

Look angles and ranges were calculated prior to the test based on the anticipated launch profile, and the instantaneous slope ($\partial \bar{A} / \partial R$) was predicted as a function of time after liftoff (shown in Fig. 2). The planned trajectory was not available prior to launch, so the profile for insertion into a similar orbit was used for planning purposes. Slope was estimated using finite differences between discrete model points. The expected trajectory quickly takes the rocket to large elevation angles (as viewed from ISTEf) and high altitudes, both of which degrade accuracy. Based on this analysis, range accuracy was expected to degrade rapidly after the first 30 s of flight, with ranging becoming impossible about 85 s after liftoff. For the longest flight times, the altitude exceeds 50 km, and the remaining thin atmosphere provides little additional absorbance. When the sensitivity of absorbance to range, $\partial \bar{A} / \partial R$, decreases to 10^{-4} , a minimum detectable absorbance of $\bar{A} = 10^{-2}$ yields an approximate range error of 100 km.

RESULTS AND ANALYSIS

Lamp Experiments. Atmospheric absorption near 762 nm with the rotational structure of the O_2 ($X^3\Sigma_g^- \rightarrow b^1\Sigma_g^+$) (0,0) transition is simulated using the line-by-line radiative transfer model (LBLRTM) and the high-resolution transmission molecular absorption (HITRAN) database in Fig. 3.⁸ The spectrum exhibits four rotational branches ($\Delta^K \Delta J = {}^P P, {}^P Q, {}^R R, {}^R Q$) described by Hund's case (b) for a magnetic dipole transition. The population of absorbers in different rotational states is temperature dependent, and the line shape is a function of both pressure and temperature. As a result, the absorption at a given frequency is a function of atmospheric conditions at each point along the path. The frequency dependent absorption, $A(\bar{\nu})$, after propagating over a range R is defined by the Beer–

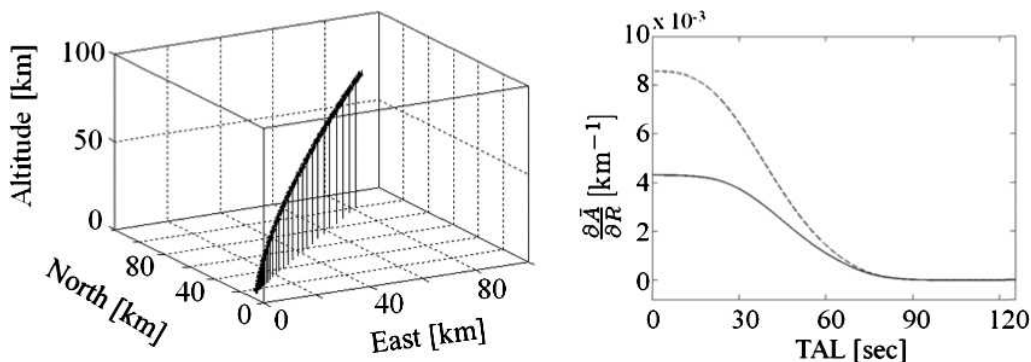


FIG. 2. (Left) launch trajectory used for planning purposes. The sensor is at the origin and the vertical bars are on 5 s intervals. (Right) Predicted slope ($\partial\bar{A}/\partial R$) for the NIR band (dashed line) and visible band (solid line) as a function of time after liftoff.

Lambert Law as

$$A(\bar{\nu}, R) \equiv 1 - \frac{I(\bar{\nu}, R)}{I(\bar{\nu}, 0)} = 1 - \exp\left(-\int_0^R \sigma(\bar{\nu}, r) N(r) dr\right) \quad (1)$$

where I represents the intensity, dr is an incremental distance along the path, and N is the absorber concentration. The attenuation cross-section, σ , would in general include effects of both absorption and scattering, but it will be shown below that only oxygen absorption will be important for this method. In general the atmospheric oxygen concentration will not be constant along the path, $N(r)$.

A spectrum of 500 W halogen lamp observed through 41 m atmospheric path and acquired with the MR254 Fourier transform infrared spectrometer (FT-IR) at 1 cm^{-1} resolution is shown in Fig. 4. The spectral resolution is adequate to completely resolve the rotational features in the P and Q branches. The average absorption over some bandwidth $\Delta\bar{\nu}$,

$$\bar{A}(R) \equiv \frac{1}{\Delta\bar{\nu}} \int_{\Delta\bar{\nu}} A(\bar{\nu}, R) d\bar{\nu} \quad (2)$$

is used to estimate the range. The band-average absorption, \bar{A} , is estimated from the observed spectra by using the out-of-band intensity to estimate the effect of all slowly varying (over $\bar{\nu}$) contributions. Observed spectra will include effects of not only absorption, but also scattering, source spectrum, and instrument response. Because the $O_2(X \rightarrow b)$ bands are spectrally isolated we can estimate a baseline signal level by interpolating across the band. Any difference between the measured signal and the baseline is assumed to be caused by oxygen absorption. The estimated value of absorption due to molecular absorption alone is then

$$A(\bar{\nu}) \simeq 1 - \frac{I(\bar{\nu})}{b(\bar{\nu})} \quad (3)$$

where I represents the measured spectrum and b is the fit baseline. The baseline value can be computed by fitting a simple quadratic polynomial through the out-of-band data. The bands used for this baseline fitting are summarized in Table I. The P-branch of the visible band does overlap with a weak water band, so the baseline here is extrapolated from higher

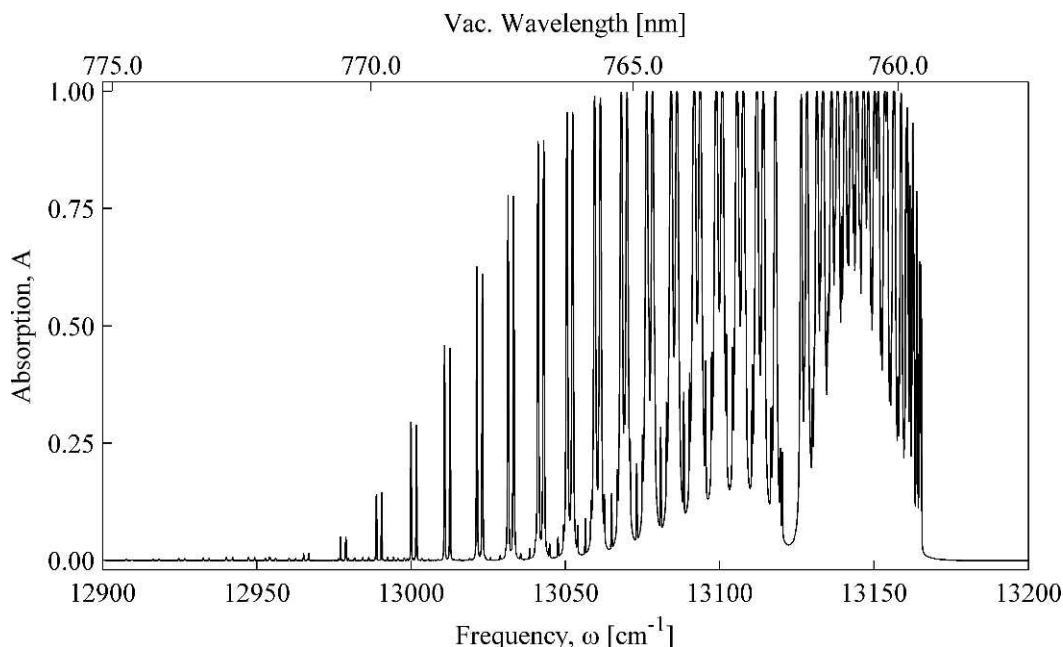


FIG. 3. Sample $O_2(X \rightarrow b)$ (0,0) absorption spectrum, computed using LBLRTM for 25 km horizontal path and a sensor 5 km above ground.

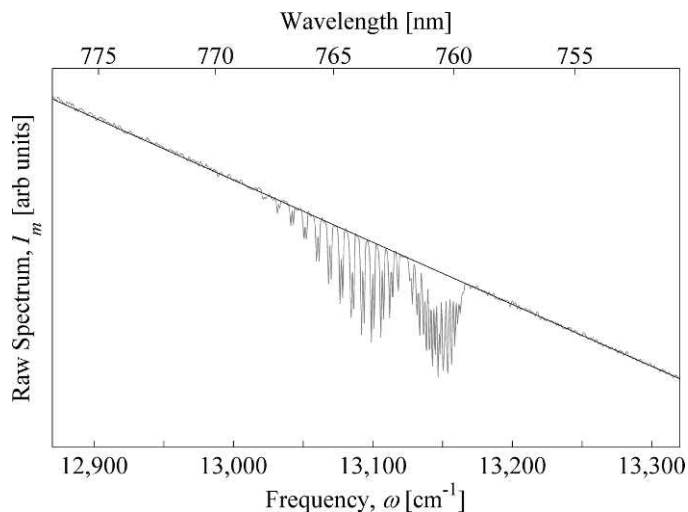


FIG. 4. Raw spectrum (gray line) of 500 W halogen lamp observed through 41 m atmospheric path showing the calculated value of the baseline (black line) inferred from out-of-band data.

frequencies. In the near infrared (NIR) band we often use only the R-branch of the band to avoid the potassium D emission doublet, as will be seen below. These band choices are somewhat arbitrary, but varying band limits has been experimentally found to have negligible impact on the accuracy of range estimates.

While the monochromatic absorption of Eq. 1 follows a simple exponential curve when plotted as a function of absorber depth, the band-averaged value obeys a subtly different shape historically known as the curve of growth.¹¹ Examples of this are shown in Fig. 5. Note that these curves differ from the traditional curve of growth, which describes absorption along a homogeneous path, while Fig. 5 also includes effects of changing concentration along the path. For the purposes of this paper, all plots of \bar{A} as a function of R will be referred to as curves of growth. The passive ranging solution technique is unique in the sense that the curve of growth is single valued.

Equation 2 applies whenever the spectral resolution (or filter bandwidth) is large compared with the transition line width. If the sensor is designed so that the band includes all rotational lines, the resulting average will be insensitive to the rotational distribution, and the cross-section can be treated as temperature independent. Note that this can be accomplished by using the entire band or by taking only the R- or P-branch, which will be important for some cases to be discussed shortly.

Because Eq. 2 cannot be directly solved to find range from observations of \bar{A} , the solution proposed here is to simply compare observed values against this curve of growth—the range at which the measured absorption intersects the curve is the range estimate. The curves can be computed numerically (using LBLRTM or MODTRAN),¹² or by interpolating historical data.

TABLE I. Band limits (in cm^{-1}).

O ₂ band	Out-of-band data (used to fit baseline)	In-band data (bounds of integral in Eq. 2)
Visible (X : 0 → b : 1)	14 590–14 900	14 527–14 566
NIR (X : 0 → b : 0)	12 785–12 843 and 13 200–13 360	13 122–13 200

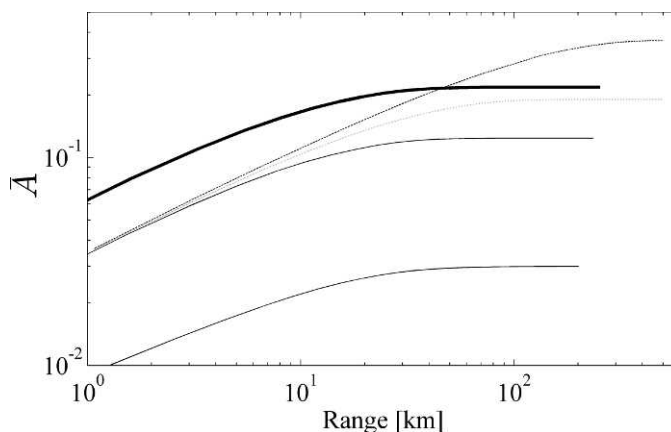


FIG. 5. Example curves of growth for five different cases computed using LBLRTM. Averages are over the entire (0,0) band. The three solid lines are for paths at 75° zenith angle and sensor altitudes of 5 km (heavy line), 10 km (black), and 25 km (gray). For 10 km sensor altitude, plots are also shown for zenith angles of 91° (dashed) and 85° (dotted).

In these lamp experiments, prior observations were used to create a curve of growth (using Eq. 2 and 3).¹³ New observations were then plotted against this curve, and the range of intersection was used as the range estimate. Examples of this are shown in Fig. 6. The actual range from sensor to target in this example was 36.6 m. The range estimated by comparing with historical data was 37.3 ± 2.1 m. The difference between the optically estimated range and the physical measured distance is 70 cm (1.9% error), within the statistical error bounds. However, the range estimate can be further improved by noting the difference in atmospheric conditions over the two different days. Because absorption really depends on the concentration length, $m = NR$, the adjusted range estimate is

$$R' = \frac{N}{N'} R \quad (4)$$

where the O₂ concentration, N , can be estimated from standard meteorological data via the ideal gas law.¹³ We assume N is 20.95% of the total concentration of dry air (corrected for humidity), yielding a concentration ratio for the two days of $N/N' = 0.977$. With this correction the final range estimate is 36.4 ± 2.1 m and the range error is reduced to 0.4%.

Static Rocket Motor Tests. Raw spectra from the 2.8 km static rocket motor test are shown in Table II, where each spectrum represents an average over 80 scans of the interferometer (MR-254). Because this was a single event, there were no empirical data to use to create the curve of growth. The curve was instead prepared from spectra predicted using LBLRTM assuming a US Standard Atmosphere. Equation 4 was again used to correct for the difference between actual conditions and the standard atmosphere. The resulting range estimate was 2.811 km, for an error of 0.5%.

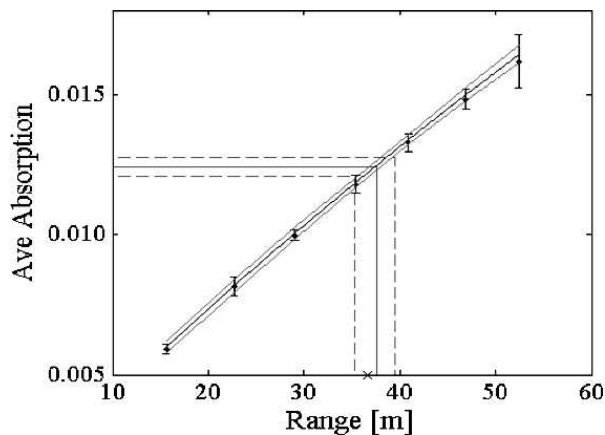


FIG. 6. Example of range estimation in short-range experiments. The points are from previous measured data; the black line is the best-fit curve of growth fit through those points (with 99% confidence interval); the horizontal gray line is the new test data (mean \pm standard deviation); the vertical gray line is the range estimated from the intersection of the average data with the metric curve. The X marks the actual range (from tape measure).

Results of the other static rocket motor tests are summarized in Table II. Note that these tests were conducted in daylight conditions, and solar scatter may systematically increase the range error in the visible bands.

Note that the rocket exhaust plume in Fig. 7 contained trace amounts of potassium, which is a contaminant in many solid propellants. The strong potassium emission doublet (D_1 at $12\,985\text{ cm}^{-1}$ and D_2 at $13\,043\text{ cm}^{-1}$) is within the P-branch region of the O_2 band. For this experiment, the band average was computed over only the R-branch ($13\,120\text{--}13\,170\text{ cm}^{-1}$) in both the measured data and the modeled spectra used to generate the curve. Because the average still includes all rotational states, the total energy in the band is still independent of temperature and instrument resolution, although the shape of the curve of growth is somewhat different.

It is also important to note that we do not use any knowledge of the source for these range estimates. The rocket propellant type was not known before or after the test. Systematic errors could be reduced if knowledge of the source radiance is available. Radiometric brightness estimates were used to help set instrument gain and integration times, but the algorithm is source independent.

The visible $O_2(X \rightarrow b)$ (0,1) band near 689 nm was nearly unusable in most static tests because (a) the band is so weak it is indistinguishable from the baseline at short range, and (b) signal-to-noise ratio (S/N) was poor at these frequencies. Even though the absolute accuracy in this band was poor, we should note that it was within the noise-based uncertainty limits predicted using Eq. 5.

TABLE II. Static test results.

Source	Actual range (km)	Source	Estimated range (km)		Error (m) (%)	
			NIR	Visible	NIR	Visible
Lamp	0.0393	Tape measure	0.0391 ± 0.0021		0.2 (0.4)	
SRM 1	2.825	GPS	2.811 ± 0.008	2.982 ± 0.07	14 (0.5)	157 (5.5)
SRM 2	0.90	Google Earth	0.876 ± 0.11	0.763 ± 0.52	24 (2.7)	137 (15.2)
SRM 3	0.90	Google Earth	0.92 ± 0.01	0.893 ± 0.01^a	10 (1.1)	7 (0.8)

^a Data in the “visible” column for SRM 3 were collected through a grating.

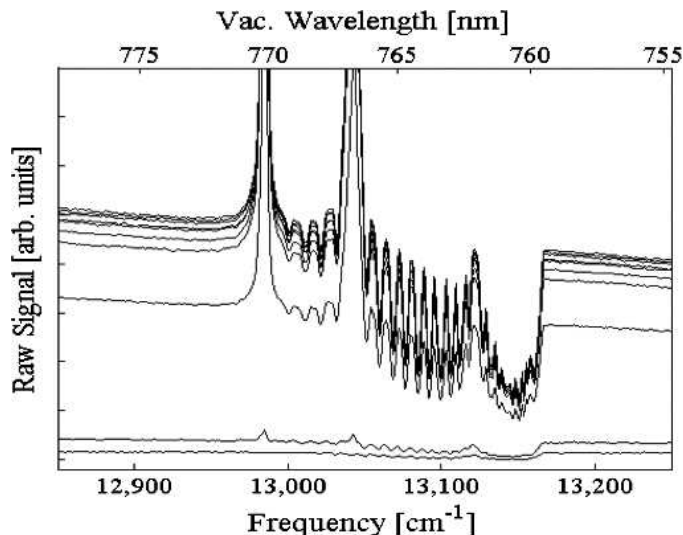


FIG. 7. Raw spectra from SRM test, showing a large potassium D_1 and D_2 emission doublet in the P-branch of the $O_2(X \rightarrow b)$ (0,1) band. Each spectrum is an average over 80 scans of the interferometer (~ 9 s) at 2 cm^{-1} resolution. At this resolution the rotational lines are well resolved, but the P - P - Q doublet for each value of J is not.

Launch Test. Figure 8 provides a sample spectrum from the Falcon 9 launch calculated by averaging over all scans from 18 to 86 s after liftoff. The rocket was not acquired until approximately 18 s after liftoff because trees obstructed the line of sight. The baseline values were fit, and values of \bar{A} were computed independently from each scan of the interferometer, using Eqs. 2 and 3. These values are shown in Fig. 9. Note the vertical scale in Fig. 9 is somewhat arbitrary—actual values will depend on the bounds chosen for the integral in Eq. 2, but the overall trend shows decreasing absorption. Even though the range is increasing with time, the density of the air along the path drops with increasing zenith angle (or source altitude), so the net effect is decreasing concentration length. Figure 9 also shows the S/N, where noise is estimated from the random variations of the measured spectrum about the best-fit line in the out-of-band data. Because most noise processes occur in interferogram space, noise is assumed to be distributed evenly in the spectrum.

Figure 10 shows predictions of \bar{A} as a function of both range and sensor zenith angle (i.e., measured from zenith, such that 0 degrees is looking straight up and 90 degrees is horizontal). This example is based on an LBLRTM model for a US Standard Atmosphere, and the band of integration in Eq. 2 is over only the R-branch of the $0 \rightarrow 0$ transition. Previous research has shown range results depend weakly on atmospheric conditions, but the correction factor of Eq. 4 that can be

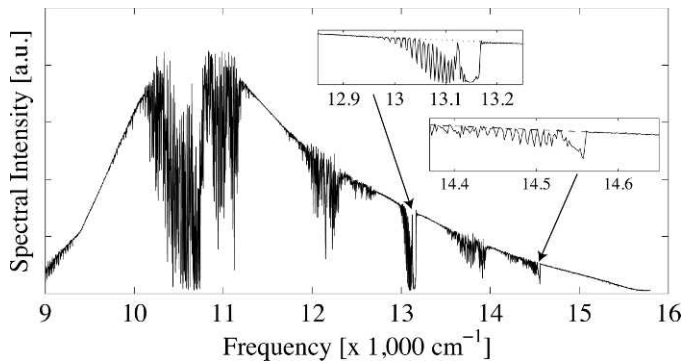


FIG. 8. Raw spectrum measured using the Bomem FTS during launch test. This is the average over 2300 scans of the interferometer (approx. 18 thru 86 s after liftoff). (Inset) Close-ups of the two O₂ bands of interest, showing the fit baseline (dotted).

derived from simple weather data (only temperature, pressure, and humidity are needed).⁹ Range accuracy is limited primarily by uncertainty in measurements of \bar{A} (i.e., noise). The uncertainty in the range estimate, σ_R , is approximately

$$\sigma_R \approx \sigma_A \left(\frac{\partial \bar{A}}{\partial R} \right)^{-1} \quad (5)$$

where σ_A is the uncertainty in \bar{A} , which in practice is estimated as the standard deviation taken over multiple data sets (spectra). Range uncertainty can become extremely large when the slope ($\partial \bar{A} / \partial R$) is near zero—i.e., if the curve in Fig. 10 is flat, a small error in \bar{A} leads to a very large error in the intercept range. This occurs either at long ranges (where the band becomes saturated) or at high target altitudes (where the absorber concentrations becomes very small). Because the visible (0,1) band is a weaker transition, the effects of saturation are generally less significant than in the NIR (0,0) band, but both suffer equally for high-altitude targets. Systematic errors may also be present. For example, an improper curve of growth may result from inaccurate atmospheric profiles or errors in pointing angles.

Figure 11 shows the range estimated by comparing the values of \bar{A} in Fig. 9 against curves of growth such as the one

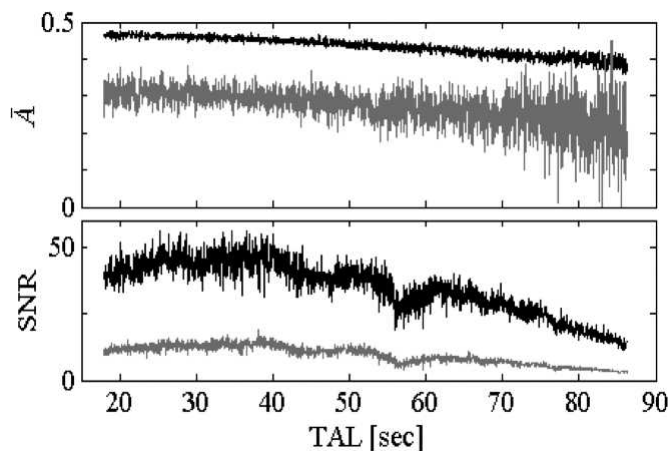


FIG. 9. (Top) Measured values of band-average absorption computed from the visible band (gray) and the NIR band (black). (Bottom) signal-to-noise ratio for each band, where noise is estimated from RMS deviation about the fit baseline.

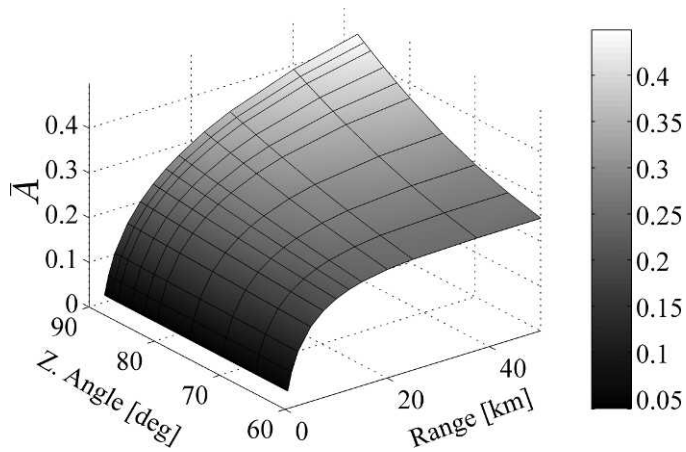


FIG. 10. Model predictions of \bar{A} as a function of zenith angle and range for the visible (0,1) band. Note how the curve flattens at long range, particularly for up-looking (lower zenith angle) cases.

shown in Fig. 10. This shows a slight bias toward underestimating range in the visible band, particularly at later times. Results for the NIR band consistently overestimated range. Reasons for this are not yet known. One possible cause is scattered sunlight. This could affect the NIR band more than the visible band because of the differential reflection from the dense vegetation surrounding the sensor. Scattered sunlight has traveled much further through the atmosphere than light originating from the rocket plume, so this would lead to an overestimation of range. Without further experimentation, it is impossible to definitely attribute the source of this error.

The measurement noise illustrated in Fig. 9 limits the accuracy of this technique. Equation 5 was used to calculate expected limits on range accuracy by combining the observed variance in \bar{A} with model-predicted values of slope. The standard error in \bar{A} was computed by fitting a low-order polynomial through the absorption values shown in Fig. 9 then

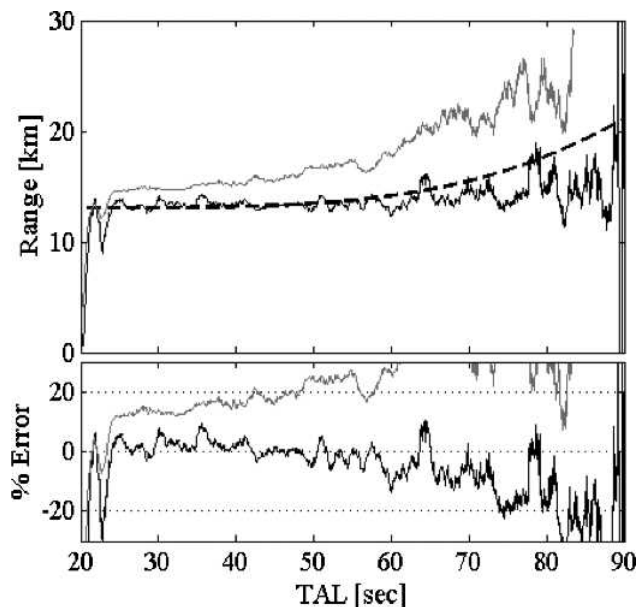


FIG. 11. (Top) Range estimated from visible (black line) and NIR (gray line) band absorption, compared to the best estimate of trajectory (dashed line). (Bottom) Range error for each band.

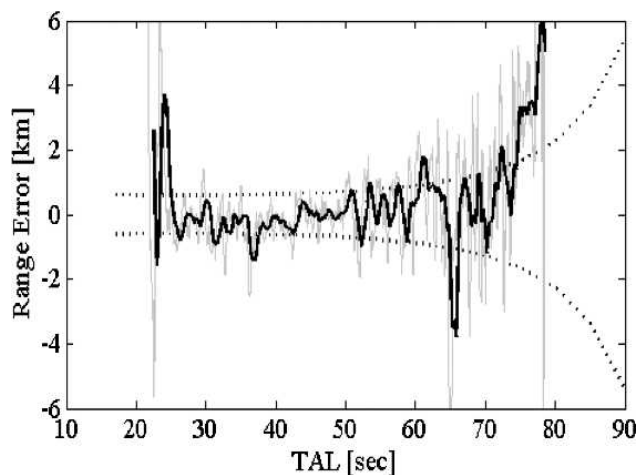


Fig. 12. Range uncertainty predicted from Eq. 5 (dotted lines) and measured range error from visible band data (gray line). The black line shows a 1 s moving average in visible band data.

computing the root mean square (RMS) error from that line. This constant estimate of error ($\sigma_{\bar{A}}$) was multiplied by the slope of the $\bar{A}(R)$ curves calculated for the actual zenith angles and ranges (taken from the best estimate of trajectory [BET] data provided by the test range based on multiple tracking sensors). This predicted accuracy limit is shown in Fig. 12 for the visible band, along with the actual error relative to BET. The peak S/N in this test was about 15 for the visible band data, so a 1.5 s moving average was used to reduce noise in the spectra prior to computing absorption as represented by the gray line in Fig. 12. The black line shows 1 s average values of range. With averaging, the range estimate is within the predicted error bars 75% of the time. The predicted error bars shown are based on twice the standard deviation, which should predict a 95% confidence interval if the noise is zero mean and normally distributed, and if noisy measurements were the only source of error. While range error was large in this test, the goal here is to show consistency with the predictions of Eq. 5 in order to build confidence in our performance predictions for other engagement scenarios.

The research grade FT-IR system used in the present study is not suitable for a deployable system. Recently we develop a portable system by coupling an intensified charge-coupled device (CCD) array to a variable bandpass liquid crystal display filter and a 3.5–8.8 degree field of view optics. This deployable system was recently flight tested against an F-16 in afterburn.¹⁴

CONCLUSIONS

We have demonstrated a molecular oxygen passive ranging technique against a realistic target. Range error was below 10% for much of the rocket boost and within theoretical limits for the sensor and viewing geometry. This required no prior knowledge of the target or detailed atmospheric soundings. Range accuracy is limited primarily by measurement error (noise). Given some reasonable assumptions about sensor performance, we predict a high-altitude sensor should provide accurate range estimates at ranges over 50 km.

The visible band is weaker (i.e., lower A at a given range), which may be helpful in reducing the effects of saturation. This advantage is largely offset in these results by the reduced modulation efficiency of our interferometer at higher frequencies. For other instruments, the visible band may be preferred.

Future efforts will be aimed at developing a sensor that will (1) perform better in the visible and NIR bands than the FTS used so far and (2) be consistent with the requirements for a flight test. Because band averages are the primary figure of merit, a simple bandpass filter system may be possible. Some algorithm improvements will also be investigated, such as use of other bands (perhaps 13 400–14 000 cm^{-1}) to estimate the H_2O concentration length and correct for the water band interfering with the visible $\text{O}_2(X \rightarrow b)$ (0,1) band.

ACKNOWLEDGMENTS

Portions of this work were funded by the National Air and Space Intelligence Center (NASIC). Special thanks are also due to Space-X and the 45th Space Wing for providing the best estimate of trajectory.

1. G.P. Perram, S.J. Cusumano, R.L. Hengehold, S.J. Fiorino. An Introduction to Laser Weapon Systems. Albuquerque, NM: Directed Energy Professional Society, 2009.
2. T.J. Slusarchyk, J.C. Davis, J.J. Lisowski, J. Kiessling. "Monocular Passive Ranging in Support of Ascent Phase Ballistic Missile Intercepts". Proc. Military Sensing Symposium (MSS:MDSEA). 2009.
3. B.J. Steward, G.P. Perram, K.C. Gross. "Visible and Near-Infrared Spectra of the Secondary Combustion of a 152mm Howitzer". Appl. Spectrosc. 2011. 65(12): 1363-1371.
4. A.N. Steinberg. "Sensor and Data Fusion". In: J.S. Accetta, D.L. Shumaker, editors. The Infrared and Electro-Optical System Handbook. Bellingham, WA: SPIE Press, 1993. Vol. 8. Pp. 309-341.
5. B. Sridhar, R. Suorsa. "Comparison of Motion and Stereo Methods in Passive Ranging Systems". IEEE Trans. Aerosp. Electron. Syst. 1991. 27(4): 741-746.
6. J.S. Draper, S. Perlman, C.K. Chuang, M. Hanson, L. Lillard, B. Hibbeln, D. Sene. "Tracking and Identification of Distant Missiles by Remote Sounding". Proc. IEEE Aerosp. Conf. 1999. 4: 333-341.
7. K.S.W. Champion, A.E. Cole, A.J. Kantor. "Standard and Reference Atmospheres". In: A.S. Jurra, editor. Handbook of Geophysics and the Space Environment. Cambridge, MA: Air Force Geophysics Laboratory, 1985. Chap. 14.
8. L.S. Rothman, D. Jacquemart, A. Barbe, D. Chris Benner, M. Birk, L.R. Brown, M.R. Carleer, C. Chackerian Jr., K. Chance, L.H. Coudert, V. Dana, V.M. Devi, J.-M. Flaud, R.R. Gamache, A. Goldman, J.-M. Hartmann, K.-W. Jucks, A.G. Maki, J.-Y. Mandin, S.T. Massie, J. Orphal, A. Perrin, C.P. Rinsland, M.A.H. Smith, J. Tennyson, R.N. Tolchenov, R.A. Toth, J. Vander Auwera, P. Varanasi, G. Wagner. "The HITRAN 2004 molecular spectroscopic database". J. Quant. Spectrosc. Radiat. Transfer. 2005. 96(2): 139-204.
9. M.R. Hawks, G.P. Perram. "Passive Ranging of Boost-Phase Missiles". Proc. SPIE. 2007. 6569: 65690G.
10. R.A. Vincent, M.R. Hawks. "Passive Ranging of Dynamic Rocket Plumes Using Infrared and Visible Oxygen Attenuation". Proc. SPIE. 2011. 8052: 80520D.
11. R.M. Goody, Y.L. Yung. Atmospheric Radiation. New York, NY: Oxford University Press, 1989. 2d ed.
12. S.A. Clough, M.W. Shephard, E.J. Mlawer, J.S. Delamere, M.J. Iacono, K. Cady-Pereira, S. Boukabara, P.D. Brown. "Atmospheric Radiative Transfer Modeling: A Summary of the AER Codes". J. Quant. Spectrosc. Radiat. Transfer. 2005. 91(2): 233-244.
13. M.R. Hawks. "Passive Ranging Using Atmospheric Oxygen Absorption Spectra". [Ph.D. Dissertation]. Wright-Patterson AFB, OH: Air Force Institute of Technology, 2006.
14. J.R. Anderson, M.R. Hawks, K.C. Gross, G.P. Perram. "Flight Test of an Imaging $\text{O}_2(X-b)$ Monocular Passive Ranging Instrument". Proc. SPIE. 2011. 8020: 802005.